CHEMISTRY OF MATERIALS

pubs.acs.org/cm

Article

Toward Better Stability and Reversibility of the Mn^{4+}/Mn^{2+} Double Redox Activity in Disordered Rocksalt Oxyfluoride Cathode Materials

Yasaman Shirazi Moghadam, Abdel El Kharbachi,* Thomas Diemant, Georgian Melinte, Yang Hu, and Maximilian Fichtner*

Cite This: *Chem. Mater.* 2021, 33, 8235–8247

Read Online

ACCESS | Metrics & More | Article Recommendations | Supporting Information

ABSTRACT: Cation-disordered rocksalt (DRS) materials have shown good initial reversibility and facile Li^+ insertion and extraction in the structure at high rates. However, all of the Li-rich oxyfluorides introduced so far suffer from short cycle lifetimes and severe capacity fading. In the current study, we combine the strategy of using high-valent cations with partial substitution of oxygen anions by fluorine ions to achieve the optimal Mn^{4+}/Mn^{2+} double redox reaction in the composition system $Li_2Mn_{1-x}Ti_xO_2F$ ($0 \leq x \leq 2/3$). While Ti-rich compositions correlate to an O-oxidation plateau and a partial $Mn^{3+}-Mn^{4+}$ redox process at high voltages, owing to the presence of Ti^{3+} in the structure, a new composition $Li_2Mn_{2/3}Ti_{1/3}O_2F$ with a lower amount of Ti shows better electrochemical performance with an initial high discharge capacity of 227 mAh g^{-1} (1.5–4.3 V window) and a Coulombic efficiency of 82% after 200 cycles with a capacity of 136 mAh g^{-1} (>462 Wh kg^{-1}). The structural characteristics, oxidation states, and charge-transfer mechanism have been examined as a function of composition and state of charge. The results indicate a double redox mechanism of Mn^{4+}/Mn^{2+} in agreement with Mn–Ti structural charge compensation. The findings point to a way for designing high-capacity DRS materials with multi-electron redox reactions.

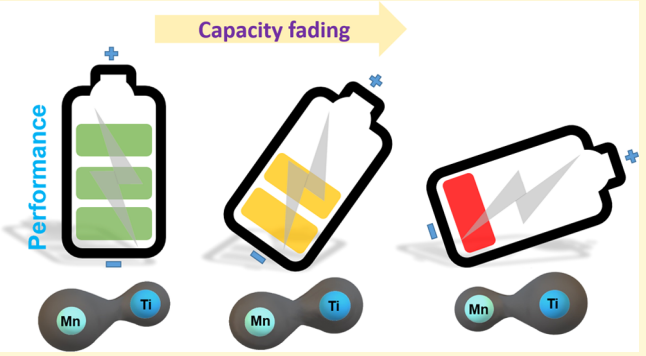

INTRODUCTION

The need for cost-effective, environmentally friendly, high-energy-density cathode materials for lithium-ion batteries (LIBs) is driven by the rapidly growing demand for efficient energy storage. Nickel and cobalt as electrochemically active transition metals in layered rocksalt materials such as Ni-rich layered oxides (e.g., $LiNi_{3/5}Mn_{1/5}Co_{1/5}O_2$) are present in most of the commercialized LIBs. Due to safety issues as well as limited resources, alternative materials are highly desirable.[1−3] Furthermore, the reversible specific capacity of a cathode material based on the cationic redox reaction of a transition metal (Ni^{4+}/Ni^{2+} and/or Co^{4+}/Co^{3+}) is limited.[3−7] As potential alternatives, disordered rocksalt systems based on vanadium and its double redox reactions have been investigated recently. Li_2VO_2F, $Li_3V_2O_5$,[5] and Li_2VO_3[6] showed high capacity and high energy density. However, vanadium is a toxic and expensive element that may be a hindrance for large-scale production, and the systems suffered from thermodynamic instabilities and fast degradation.[8,9] Hence, high-capacity cathode materials based on, e.g., manganese, could be a suitable substitution due to the low cost, low toxicity, and abundance of the element in nature.[10]

To date, several cathode compositions based on manganese have been introduced and investigated such as Li_2MnO_3, $LiMnO_2$, and $Li_4Mn_2O_5$, but their performance was limited by anionic redox issues, which have been reported to reduce the lifespan of the battery.[11−13]

As a perspective for mitigation of the issues, density functional theory (DFT) calculations have shown that titanium as a light $3d^0$ transition metal may stabilize the structure.[14,15]

Disordered rocksalt structures with achievable high capacity, due to lithium transport through percolating zero transition metal pathways, which remain active upon the delithiation process, are noticeable.[16,17] Zero transition metal diffusion paths are energetically favorable since activated lithium ions in tetrahedral sites perceive less electrostatic repulsion as a limiting diffusion barrier.[16−21] Further strategy to achieve high reversible capacity, along with high-valent Ti substitution, is O^{2-} replacement by F^-.[8,22,23] Fluorine substitution introduced by Chen et al. can reduce the average valence requirement on

Received: July 6, 2021
Revised: September 20, 2021
Published: October 18, 2021

https://doi.org/10.1021/acs.chemmater.1c02334
Chem. Mater. 2021, 33, 8235–8247

the anions, which is one of the keys to access the high level of active Li and hence reach the long-term reversible capacity of batteries.[8,24,25] Another advantage of fluorination is that it alleviates the irreversible anionic redox reaction of oxygen. In this structural regime, the lifetime of the cathode material can be increased, thereby reaching higher capacities based on cationic redox reactions.[22,26] To date, different manganese-based structures such as partially ordered spinel-like $Li_{1.68}Mn_{1.6}O_{3.7}F_{0.3}$ and Li_2MnTMO_2F (TM: Nb, Ti) disordered rocksalt have been fluorinated, proving an electrochemical improvement with respect to high energy density and better rate capability in comparison with nonfluorinated samples.[2,27]

Here, we report our study on the beneficial effect of titanium substitution on the stabilization of the disordered rocksalt structure of $Li_2Mn_{1-x}Ti_xO_2F$ ($0 \le x \le 2/3$) as a potential cathode material for next-generation Li-ion batteries. Using high-energy mechanochemical ball milling starting from equal valence Ti(III) and Mn(III),[28−30] we successfully synthesized a series of mixed-valence compounds $Li_2Mn^{III}O_2F$, $Li_2Mn_{1/3}{}^{II}Mn_{1/3}{}^{III}Ti_{1/3}{}^{IV}O_2F$, $Li_2Mn_{1/2}{}^{II}Ti_{1/2}{}^{IV}O_2F$, and $Li_2Mn_{1/3}{}^{II}Ti_{1/3}{}^{III}Ti_{1/3}{}^{IV}O_2F$, referred to as 0% Ti, 33% Ti, 50% Ti, and 66% Ti, respectively. The combined presence of high-valent Ti^{4+} as a $3d^0$ transition metal, which promotes the formation of a disordered rocksalt structure, and low-valent F^- sets up the charge balance to favor the incorporation of Mn as Mn^{2+} in the structure, allowing a Mn^{4+}/Mn^{2+} double redox reaction.[31] The chemistry, structure, homogeneity, elemental distribution, and chemical state of the prepared powder materials have been investigated using X-ray diffraction (XRD), Rietveld refinement analysis, electron microscopy, and X-ray spectroscopic techniques (XPS, X-ray absorption near-edge spectroscopy (XANES)). Subsequently, the electrochemical analyses are presented and discussed with respect to the properties of the materials.

EXPERIMENTAL SECTION

Material synthesis. $Li_2Mn_{1-x}Ti_xO_2F$ ($0 \le x \le 2/3$) powders were synthesized by high-energy mechanochemical ball milling in two steps. First, Li_2O (99.7%), Mn_2O_3 (99%), and Ti_2O_3 (99.8%, all from Alfa Aesar) were mixed in stoichiometric ratios under an inert atmosphere using a silicon nitride jar (80 mL) and balls (10 mm) as grinding media, with a constant ball-to-powder weight ratio of 25:1. The powders were milled together for 20 h (with 10 min rest after each 30 min milling interval) at a rotation speed of 600 rpm (Fritsch P6 planetary ball mill). In the second step, LiF (99.9%) was added in a stoichiometric ratio to the mixture, and the powders were milled under the same conditions for additional 20 h at 600 rpm.

Material Characterization. Powder X-ray diffraction (XRD) patterns were collected in a 2θ range of 10−45° using a STOE STADI-p diffractometer in transmission geometry with Mo $K_{\alpha 1}$ radiation (0.70932 Å), equipped with a DECTRIS MYTHEN 1 K strip detector. To avoid air exposure, all measurements were carried out with an airtight sample holder fitted with an acetate foil window. Rietveld refinement of the XRD patterns, recorded for longer times (16 h), was performed using FullProf software. For the illustration of the crystal structures, VESTA software was used.

The morphology of the as-prepared powders was determined by scanning electron microscopy (SEM, ZEISS GEMINI Crossbeam 350 field emission SEM) with in-lens detection at 5 keV. The samples were deposited on a carbon tape substrate and transferred to the SEM using an argon-filled sample transfer shuttle. Energy-dispersive X-ray spectroscopy (EDX) elemental mapping was performed with an OXFORD XMAX 50 detector at 10 kV and Aztec software.

For transmission electron microscopy (TEM) measurements, the samples were prepared inside a glovebox and transferred to the microscope without exposure to air using a vacuum transfer holder. The dry powder was directly dispersed on a TEM holey carbon membrane without the use of solvents. The measurements were performed using a Themis300 electron microscope working at 300 kV and equipped with a DCOR probe corrector and a Super X EDX detector. The K-lines of O, F, Ti, and Mn were used for quantification in scanning transmission electron microscopy (STEM)-EDX. Inductively coupled plasma-optical emission spectrometry (ICP-OES) was performed for quantitative elemental analysis of the as-prepared samples with different Ti contents (33% Ti, 50% Ti, and 66% Ti). Owing to the low solubility of Ti-based entities, 15 mg of each powder was dissolved overnight in concentrated aqua regia and the diluted samples were subjected to ICP-OES analysis.

The chemical state of the elements in the topmost surface layer (sampling depth ∼3−5 nm) was analyzed by X-ray photoelectron spectroscopy (XPS) measurements with a PHI 5800 Multi-Technique ESCA System (Physical Electronics). To avoid surface contamination, the samples were transferred in an inert gas atmosphere to the sample load lock of the XPS system. The measurements were carried out using monochromatized Al Kα radiation (250 W, 15 kV), a detection angle of 45°, and analyzer pass energies of 93.9 and 29.35 eV for survey and detail spectra, respectively. When necessary, the samples were neutralized with electrons from a flood gun (current ca. 3 μA). Binding energy calibration was performed by setting the C 1s main peak to 284.8 eV. Peak fitting was accomplished using the CasaXPS program package with a Shirley-type background and Gaussian-Lorentzian peak profiles.

To clarify the chemical state of Ti and Mn in the synthesized compositions, X-ray absorption near-edge spectroscopy (XANES) on Ti and Mn *K*-edges were measured for pristine $Li_2Mn_{1-x}Ti_xO_2F$ ($0 \le x \le 2/3$) compounds in transmission mode using a commercial laboratory device (easyXAFS300+, easy XAFS LLC, Renton, WA). The instrument is based on Rowland circle geometries with spherically bent crystal analyzers (SBCAs) and a silicon drift detector (AXAS-M2, KETEK GmbH, Munich, Germany).[32] A Si(400) SBCA was used for the Ti *K*-edge and Si(440) for the Mn *K*-edge. Ti_2O_3 (99.9%, 325 mesh, Sigma-Aldrich, stored in a glovebox) and TiO_2 (99.9%, anatase, 32 nm, Alfa Aesar) powders were used as Ti^{3+} and Ti^{4+} references. MnO (99%, 60 mesh, Aldrich), Mn_2O_3 (99%, 325 mesh, Aldrich), and MnO_2 (99.9%, 325 mesh, Alfa Aesar) powders were used as standards for Mn^{2+}, Mn^{3+}, and Mn^{4+}, respectively. These oxide powders were first thoroughly ground in an agate mortar, and then fine particles were selected by sedimentation using acetone (VMR, 99.5%). Weighed powders were mixed with 30−40 mg of cellulose and pressed into pellets of 10 mm diameter, which were then sandwiched by Kapton tapes. The calculated mass of materials leads to a 0.7−1.5 edge jump in the measured absorption spectra. Pristine $Li_2Mn_{1-x}Ti_xO_2F$ with 0, 33, 50, and 66% Ti were prepared in a similar way inside the glovebox. Kapton-tape-sandwiched pellet samples were mounted on stainless steel washers with an aperture size of 9 mm and then placed on a sample turret (ZWO/EFW), allowing remote sample changes. An empty washer with two layers of Kapton tape was used to measure the incident X-ray beam, and a 5 μm Ti metal foil and a 400 mesh Mn foil (Exafs Materials, Danville, CA 94526) were measured as references for calibrating the energy shift of Ti and Mn *K*-edges, respectively. The incident beam, transmitted X-ray for reference/standard samples, and $Li_2Mn_{1-x}Ti_xO_2F$ were measured sequentially. A resolution of 0.25 eV was used for the XANES region, and multiple scans for each sample were collected to improve the signal-to-noise ratio. $Li_2Mn_{1-x}Ti_xO_2F$ samples were freshly prepared inside the glovebox and then transported to the ambient X-ray absorption fine structure (XAFS) measurement to maintain their as-synthesized states and minimize possible time effects due to air exposure or X-ray beam damage. The absorption spectra were calculated according to the transmission relation $\mu(E) \sim \ln(I_0/I_t)$ by a python-based software (easy XAFS LLC, Renton, WA), which is also used for dead time correction and energy calibration. The calibrated absorption data were further processed using Athena and Larch software.[33,34]

Electrochemical Testing. To prepare the cathode composite, active material and Super P conductive carbon black were mixed

https://doi.org/10.1021/acs.chemmater.1c02334
Chem. Mater. 2021, 33, 8235−8247

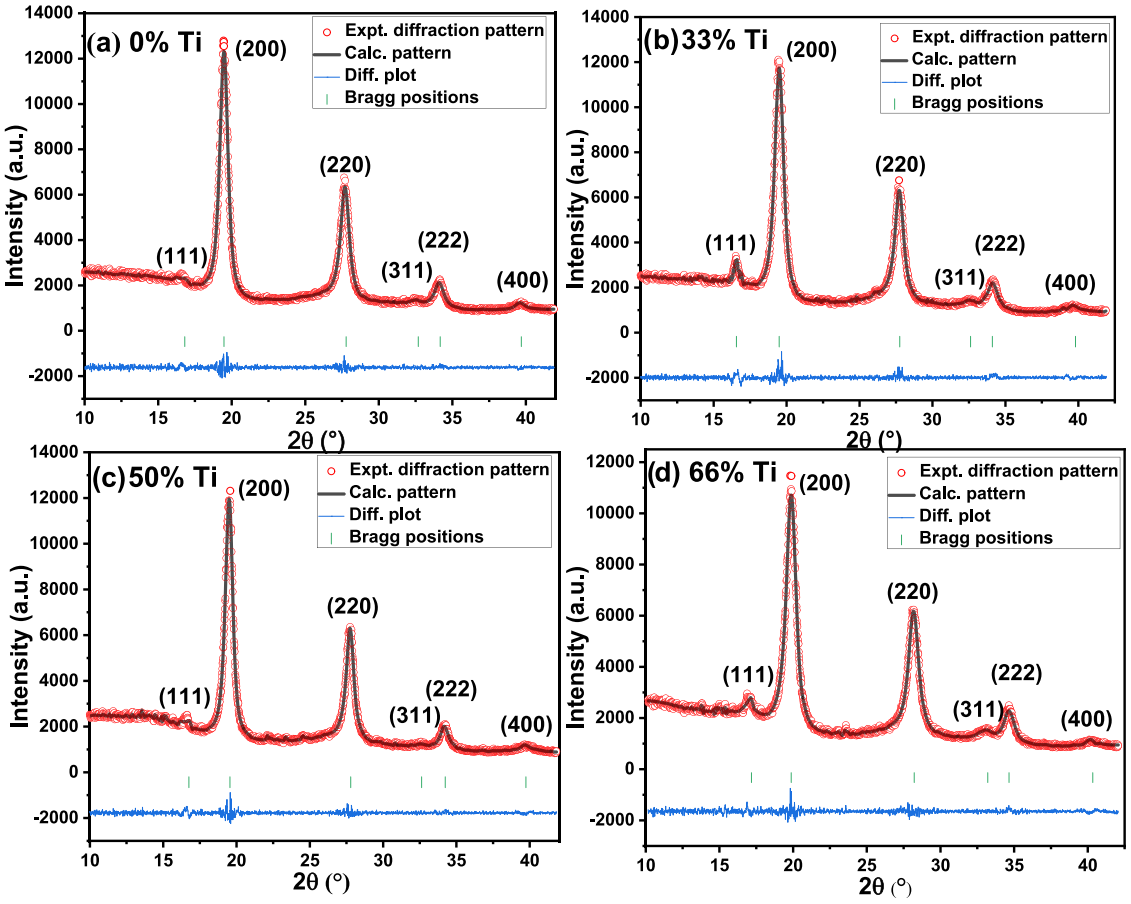

Figure 1. X-ray diffraction patterns and results of the Rietveld refinement of a cubic rocksalt phase (space group $Fm\bar{3}m$) with 0% Ti (a), 33% Ti (b), 50% Ti (c), and 66% Ti (d).

together under an inert atmosphere in a 20 mL silicon nitride jar for 3 h at 300 rpm using a Fritsch P7 premium line planetary ball mill. Coarse and agglomerated particles were removed using a 230 mesh sieve. The premixed active material and carbon black were blended with poly(vinylidene fluoride) (PVDF) as a binder with a weight ratio of 70:20:10 in 900 μL of *N*-methyl-2-pyrrolidone (NMP) for 15 min using a Thinky Mixer (ARE-250 Thinky Inc.). The mixed components were cast on an Al current collector using the doctor blade technique in an argon-filled glovebox. Subsequently, the coatings were dried in an oven located inside the glovebox at 120 °C for 12 h under vacuum. The electrodes were punched as 12 mm disks, containing around 1.5 mg of the active material each. For all of the electrochemical cells, 1 M $LiPF_6$ in an ethylene carbonate/diethyl carbonate (EC/DEC) solvent mixture (1:1, BASF) was used as an electrolyte, in the presence of Whatman glass fiber as a separator and a Li metal foil as a counter/reference electrode. Electrochemical tests were carried out in two-electrode Swagelok-type cells, assembled in an Ar-filled glovebox, and kept there for 24 h before cycling. Galvanostatic charge−discharge cycling was performed at 25 °C in a voltage range from 1.5 to 4.3 V at various C-rates using an Arbin BT2000 electrochemical cycler. All of the calculated charge and discharge capacities were based on the net active material loading in the working electrode. Cyclic voltammetry (CV) measurements for the cells were carried out in the 1.5−4 V range at different scan rates using a VMP-3 potentiostat from Bio-Logic. Electrochemical impedance spectroscopy (EIS) was carried out at 25 °C after the 2nd and 40th electrochemical cycles (in the discharge state) using the VMP-3 impedance analyzer function in a frequency range of 200 kHz−10 mHz with an AC voltage of 10 mV.

RESULTS AND DISCUSSION

Synthesis and Structural Characterization. Figure 1 shows the powder XRD patterns for the four synthesized compounds with varied Ti/(Mn+Ti) ratios. For all of the compositions, the disordered rocksalt structure was successfully formed by the mechanochemical synthesis process.[13] The broad diffraction peaks in the patterns indicate the nanocrystalline nature of the synthesized materials, which is most prominent for Ti-rich compositions (Figure S1).[35] Such structural features could result from changes in the mechanical properties upon Ti incorporation. Rietveld refinement analysis (Figure 1a−d) confirms that all of the compounds crystallize in the same cubic $Fm\bar{3}m$ symmetry (space group No. 225) with a disordered rocksalt (DRS) structure, in which Li, Mn, and Ti cations randomly occupy 4a Wyckoff octahedral sites, and O and F anions occupy 4b Wyckoff tetrahedral ones. The refinement also reveals that no significant impurities can be detected and the patterns clearly correspond to a DRS structure with low $R_{wp} \approx 1$ for the four compositions. Increasing the Ti content (0−66 atom %) correlates well to an increase of the lattice parameter from 4.1391 to 4.1934 Å (Table 1), which also affects the cell volume and crystal density. This development is consistent with the larger crystal radii of Ti(III, IV) and Mn(II) in comparison to that of Mn(III). More details on the refinements are given in the Supporting Information (SI, Table S1). Using the Williamson−Hall method, the crystallite size was calculated for the different samples, as shown in Table 1. The trend shows that

https://doi.org/10.1021/acs.chemmater.1c02334
Chem. Mater. 2021, 33, 8235−8247

Table 1. Structural Parameters of the Different Phases Based on Rietveld Refinement and SEM Analysis

composition	lattice parameter, Å	cell volume, Å^3	crystallite size, nm	average particle size, nm
0% Ti	4. 1391(5)	70.915	9 ± 2	220
33% Ti	4.1856(6)	73.330	7 ± 2	214
50% Ti	4.1899(4)	73.552	5 ± 1	172
66% Ti	4.1934(6)	73.740	3 ± 1	154

the crystallite size has an inverse relation with the Ti amount. The microstrain contribution to peak broadening was found to be less than 0.3% for all of the samples. A schematic illustration of the crystal structure of the precursors before and after the synthesis of the final DRS structure is represented in Figure 2.

The size, morphology, and chemical mapping of the particles of the four samples were investigated by SEM (Figure S2) and high-angle annular dark-field (HAADF) STEM imaging (Figure 3), both combined with EDX. Small primary particles together with nanosized aggregates having different shapes and orientations formed polycrystalline particles, which were closely packed and agglomerated. Selected area electron diffraction of the 33% Ti sample clearly identified the cubic rocksalt structure, as shown in Figure 3c. The indexation of the diffraction rings is accurately consistent with the XRD diffraction results. The average primary particle size in the 0% Ti sample was around 220 nm, and Ti substitution generally led to a reduction of the particle size, which is in agreement with lower scattering domains obtained by XRD (Table 1). For direct comparison, the statistical distribution of the particle size for different compositions is presented in Figure S2e. While a normal distribution is considered for the estimation of the average particle size, a bimodal trend may also be followed. The elemental compositions as derived from EDX and ICP-OES analysis are summarized in Tables S2 and S3. The obtained results corroborate the expected Ti/Mn ratios for the three mixed compounds. Depending on the technique (EDX or ICP) employed to quantify the samples, the Ti/Mn ratio may shift slightly according to the intrinsic properties of each element (mainly electronic structure and solubility). With respect to Ti/Li and Mn/Li ratios, the values remain underestimated using ICP for the same reason mentioned here. Finally, it may be noted that EDX elemental mapping revealed a uniform distribution of Mn, Ti, O, and F in all samples.

Electrochemical and Cell Tests of Cathode Composites. Figure 4 summarizes the results of the galvanostatic cycling with a potential limitation between 1.5−4.3 V to avoid the oxygen anionic redox reaction.[36] The insertion/extraction of 1 Li per formula unit during 10 h (C/10 rate) was repeatedly recorded for the 1st, 3rd, 10th, and 100th cycles for the four cathode materials. Steady sloping voltage profiles can be seen for all samples except the 66% Ti sample; the profiles present a reasonable average voltage hysteresis (around 80 mV) and stay relatively stable during cycling. The results suggest that structural changes and oxygen loss are small.[37−39] Assuming 2 Li per formula unit, the theoretical capacity increases with increasing Ti amount from 447, 456, 460 to 465 mAh g^{-1} for 0% Ti, 33% Ti, 50% Ti, and 66% Ti, respectively. In the measurements, however, the highest initial reversible capacity of 262 mAh g^{-1} belongs to the sample with 50% Ti, corresponding to the extraction of 1.24 Li per formula unit. The measured discharge capacities in the first cycle are approximately half of the theoretical values for the samples with 0% Ti (224 mAh g^{-1}) and 33% Ti (235 mAh g^{-1}) and less than half for 66% Ti (185 mAh g^{-1}), pointing at a lower degree of active Li in the structure.

It should be mentioned that in these high-valent TM oxyfluoride materials, it is common to consider the redox capacity, which corresponds to around 230 mAh g^{-1} for all of the compositions, as only 1 Li can be extracted since excessive delithiation can lead to irreversible structural changes.[40] Although excessive delithiation did not take place, all electrode materials show a significant loss of capacity upon prolonged cycling (Figure 5a). A possible reason for the capacity loss could be the dissolution of Mn ions into the electrolyte, which is a known phenomenon for many Mn-based cathodes, depending on the structural stability of each composition.[41,42]

In the early stage of cycling, the 50% Ti sample achieves the highest capacity. This can be rationalized by the fact that Ti

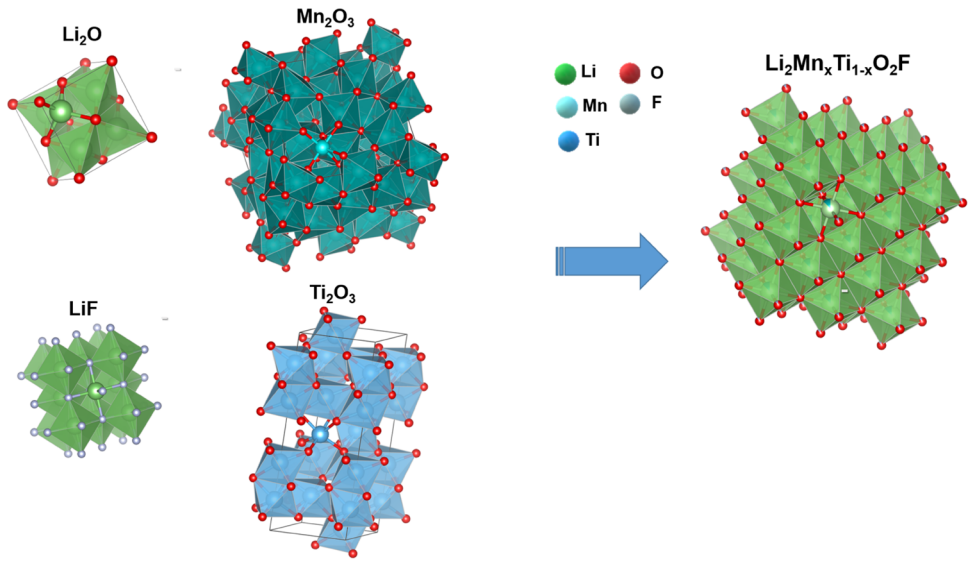

Figure 2. Schematic illustration of the crystal structure of the precursors used in the synthesis and of the obtained DRS phase.

https://doi.org/10.1021/acs.chemmater.1c02334
Chem. Mater. 2021, 33, 8235−8247

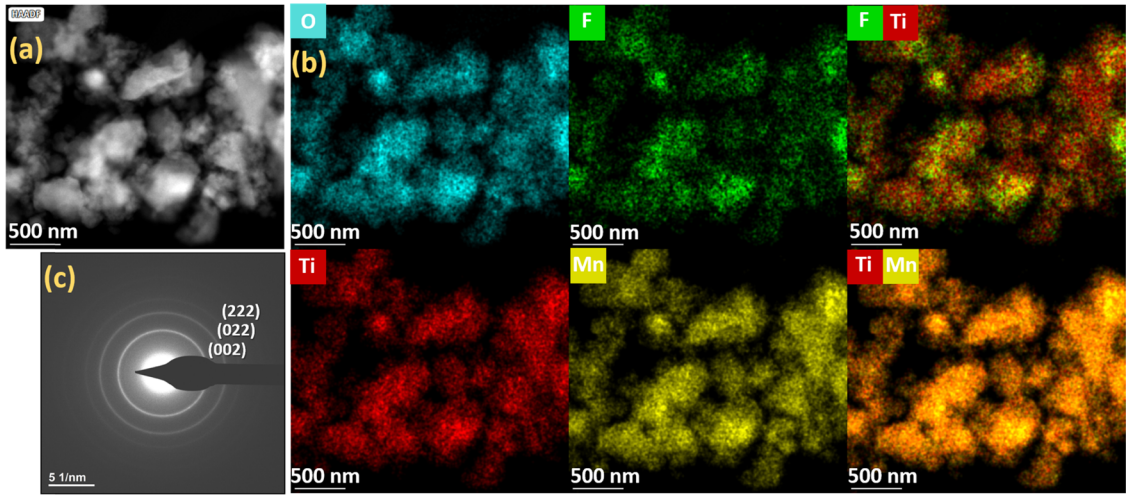

Figure 3. HAADF STEM image (a) with the corresponding EDX mapping (b) and the selected area diffraction pattern (c) of the $Li_2Mn_{2/3}Ti_{1/3}O_2F$ sample.

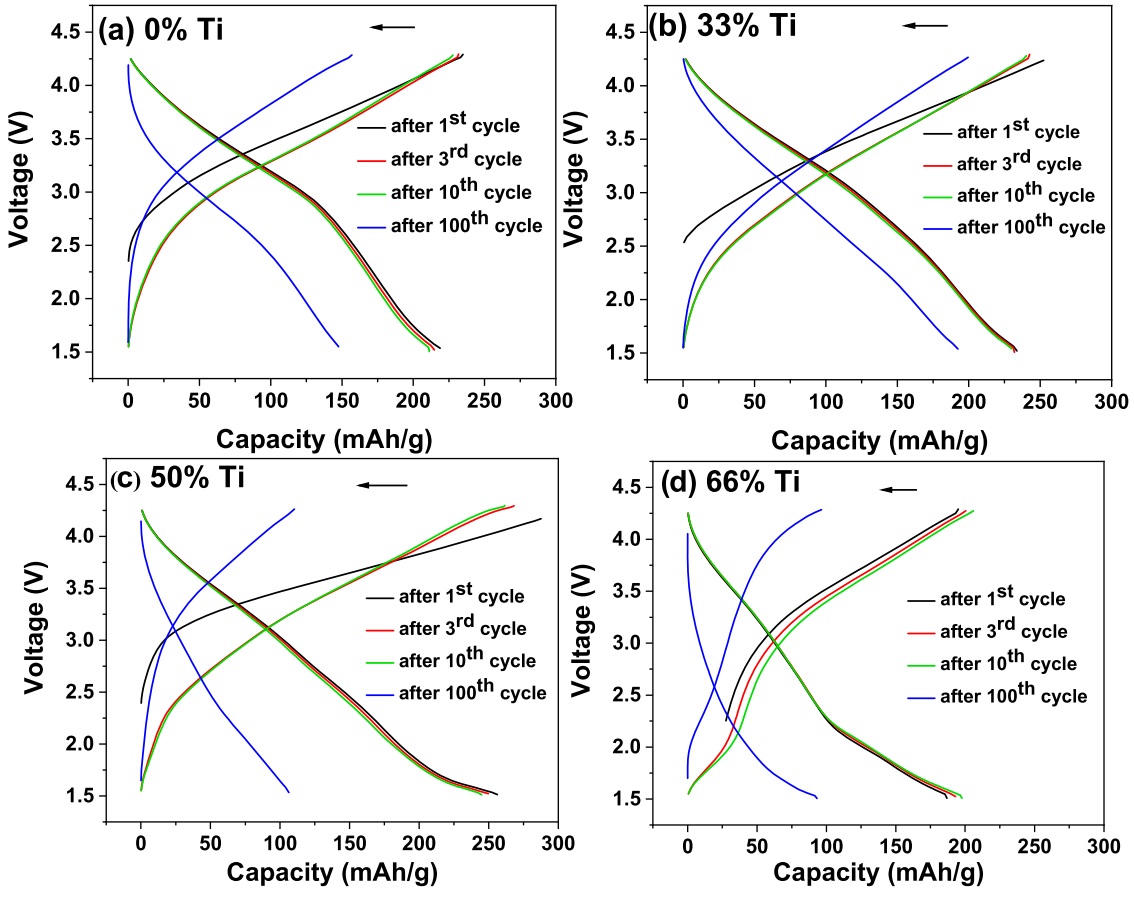

Figure 4. Voltage profiles for the 1st, 3rd, 10th, and 100th cycles of the four samples: 0% Ti (a), 33% Ti (b), 50% Ti (c), and 66% Ti (d) (voltage window: 1.5−4.3 V, 0.1C, 25 °C).

cations as $3d^0$ TM can keep all of the Mn cations in their lower oxidation state. However, this structure seems to be destabilized during prolonged cycling. It can be assumed that more Mn(II) ions are activated in the structure, which makes the dissolution more pronounced.[43] Furthermore, the beginning of the O-oxidation plateau is clearly visible for this composition, which is in agreement with previous reports, when cycling the material at high voltages.[2] Interestingly, the sample with 33% Ti shows the best capacity retention after 200 cycles, maintaining a discharge capacity of 136 mAh g^{-1} (inset of Figure 5a) with a Coulombic efficiency of around 82% and significantly smaller charge−discharge polarization (Figure 5b). Such improvement can be linked to better structural stability, as well as to the presence of the mixed valence for Mn(II, III) in comparison to the 50% Ti sample. It is noteworthy that the Ti−Mn binary phase diagram provides atomic miscibility at the Ti/Mn (1:2) ratio (SGTE database).

https://doi.org/10.1021/acs.chemmater.1c02334
Chem. Mater. 2021, 33, 8235−8247

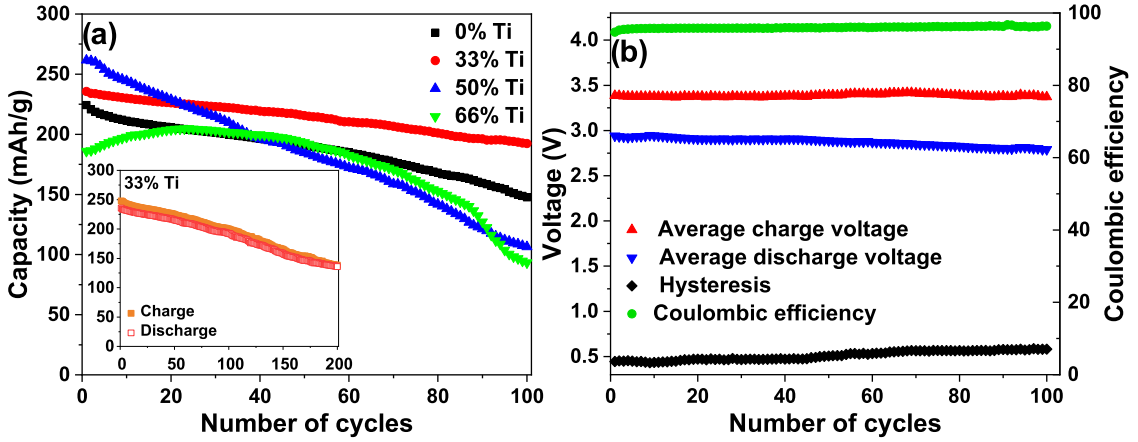

Figure 5. Comparison of the specific discharge capacity and capacity retention (a) of the four samples (0% Ti, 33% Ti, 50% Ti, and 66% Ti) as a function of cycle number (0.1C, 25 °C). The inset shows the specific charge and discharge capacity and capacity retention of the 33% Ti sample until 200 cycles. (b) Average voltage, hysteresis (ΔV), and Coulombic efficiency of the 33% Ti sample.

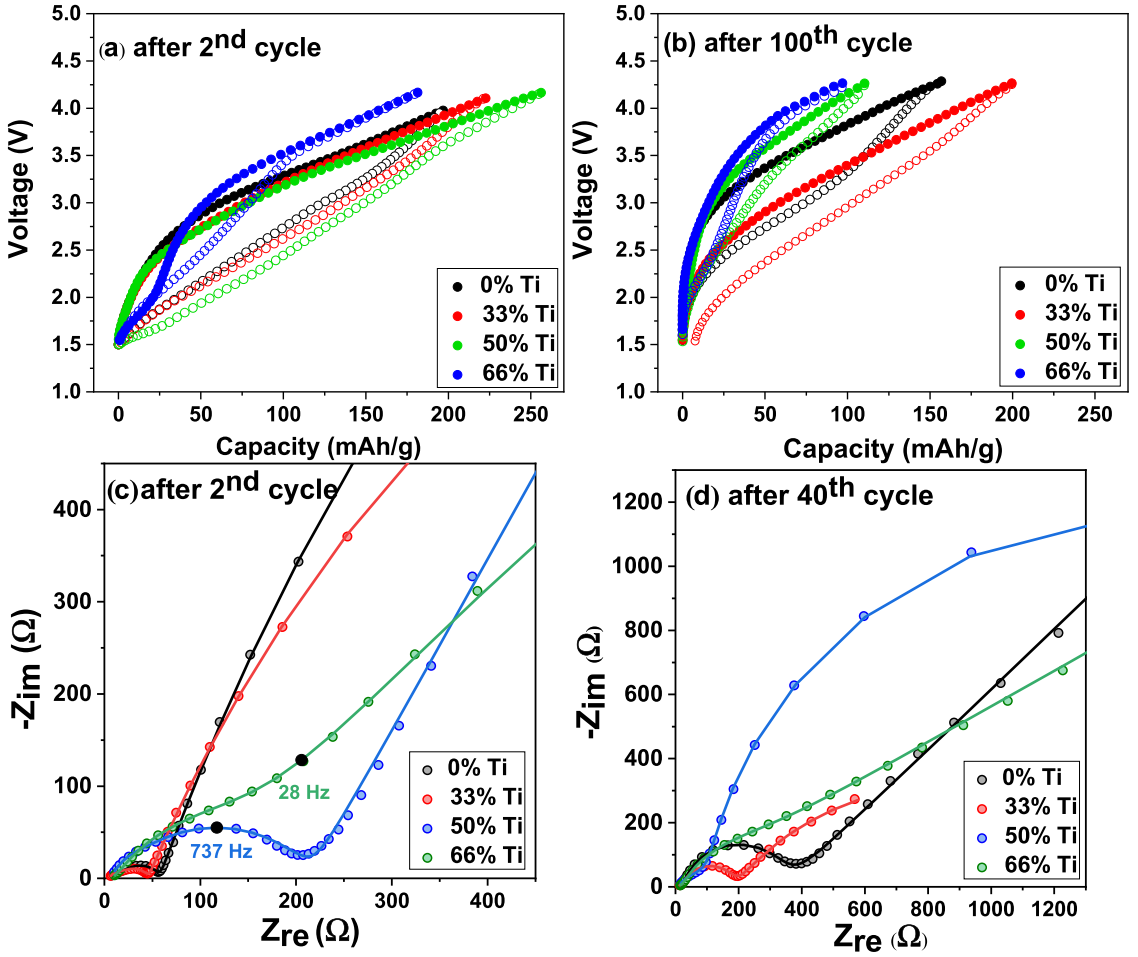

Figure 6. Circle plots of the voltage profiles for the four samples (0% Ti, 33% Ti, 50% Ti, and 66% Ti) after the 2nd (a) and 100th cycles (b), Nyquist plots of impedance after the 2nd (c) and 40th (d) cycles for the four samples. Details on the fittings and the circuit model can be found in the SI (Figure S3).

For the $Li_2Ti_{1/3}Mn_{2/3}O_2F$ composition (33% Ti), we carried out ICP-OES post-mortem analysis (Table S4) on the lithium foil anode (DMC prewashed) after prolonged cycling to detect any migration of Mn and Ti to the anode side. It can be seen that even in the best performing sample, Mn dissolution-related issues can occur, where the Mn amount is 10 times higher than that of Ti after 100 cycles. Further studies may deal with the surface coating of the particles to minimize Mn dissolution.

Besides, the 66% Ti sample shows the lowest initial capacity, presumably due to the low Mn (+II) content (33%) in comparison with the other three samples since Mn redox is the

https://doi.org/10.1021/acs.chemmater.1c02334
Chem. Mater. 2021, 33, 8235−8247

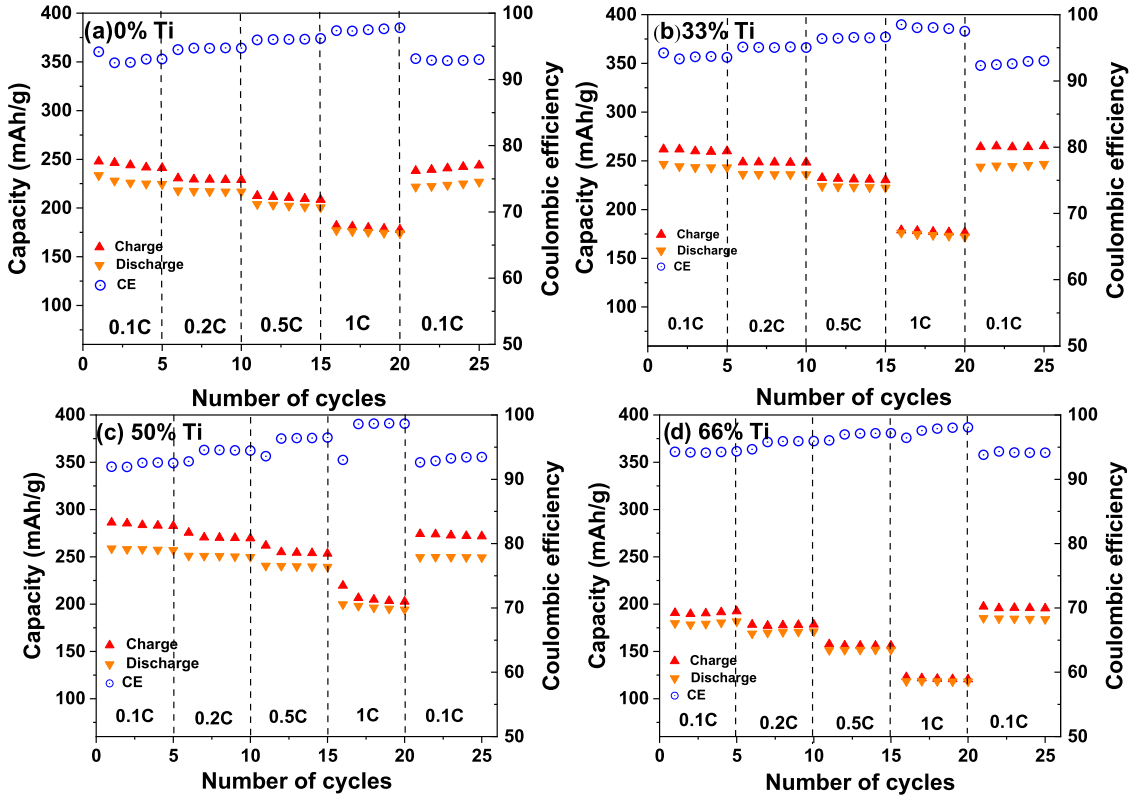

Figure 7. Rate capability comparison of the four electrodes (a) 0% Ti, (b) 33% Ti, (c) 50% Ti, and (d) 66% Ti within a voltage window of 1.5−4.3 V at 25 °C. The right axis indicates the Coulombic efficiency (CE) versus cycle number.

factor that controls capacity.[36] Figure 5 shows that the discharge capacity increases during the first 20 cycles, before decreasing again in the following cycles. It cannot be ruled out that structural modifications may occur during cycling due to the presence of Ti(III), which is thermodynamically less stable than Ti(IV). It is interesting to note that the 66% Ti sample exhibits lower working potential and higher capacity fading after 100 cycles.

Lithium ion migration within particles is promoted by the presence of short diffusion pathways, and in the case of smaller particles, diffusion can be enhanced. However, in the case of the higher activity of the material, dissolution is more likely to happen.[44−46] In our case, the reason behind the higher rates of capacity loss by increasing the Ti content might be the smaller particle size, which amplifies the dissolution of the corresponding entities in the electrolyte during cycling.[43]

The voltage versus specific capacity circle plots for the four samples after the 2nd and 100th cycles are presented in Figure 6. At both cycle numbers, shifts in capacity, charge/discharge hysteresis, and voltage slope profiles can be found. All four samples show a sloping voltage profile from the 2nd cycle; nonetheless, there is no overlap of the curves in the high voltage region. These differences can be explained by the different amounts of Mn ions taking part in the redox reaction. Owing to the small size of the particles for the four composite electrodes, redox transformations could be mitigated.[47] Regardless of Mn ion dissolution, there are always some interactions between the electrolyte and the active material that are irreversible reactions. From one side, the electrode−electrolyte interface can be stabilized after prolonged cycling, resulting in lower polarization, along with electrolyte depletion. Otherwise, these interactions can also be translated as capacity fading due to mass loss.

To get a better understanding of the electrode−electrolyte interface evolution, electrochemical impedance spectra were collected. The EIS data and correlated Nyquist plots of the four cathodes after the 2nd and the 40th cycles in the discharge state (1.5 V) are shown in Figure 6c,d, respectively. Basically, they consist of one depressed semicircle at high/middle frequencies, in addition to a Warburg tail at low frequencies. The depressed semicircle is linked to charge-transfer resistance (R_{ct}) and double-layer capacitance, while the Warburg tail is assigned to lithium diffusion.[48]

During cycling, the resistive contributions from the different segments of the batteries such as lithium ion migration through the electrode surface film, bulk resistance, and charge-transfer resistance would be increased due to the reduced stability of the electrolyte and electrode components. As can be seen based on the Warburg tail at low frequencies, there are some additional polarization processes that show that the resistance is not only due to electronic carriers but also related to the diffusion in the material.[49] A general equivalent circuit model, as shown in the inset of Figure S3a, was used to fit the EIS data. This model is better resolved for the 0% and 33%Ti samples after the 2nd cycle: an extrapolated intercept with the real Z-axis represents the ohmic resistance (R_s) of all cell components, and the following two suppressed semicircles that are partially overlapped in the high-to-medium-frequency range indicate that there are two relaxation processes with distinct time constants. The higher-frequency semicircle is attributed to the surface SEI layer (R_{sei}/C_{sei}) and the medium-frequency one is associated with charge-transfer resistance (R_{ct}) and double-layer capacitance (C_{dl}), followed by the low-

https://doi.org/10.1021/acs.chemmater.1c02334
Chem. Mater. 2021, 33, 8235−8247

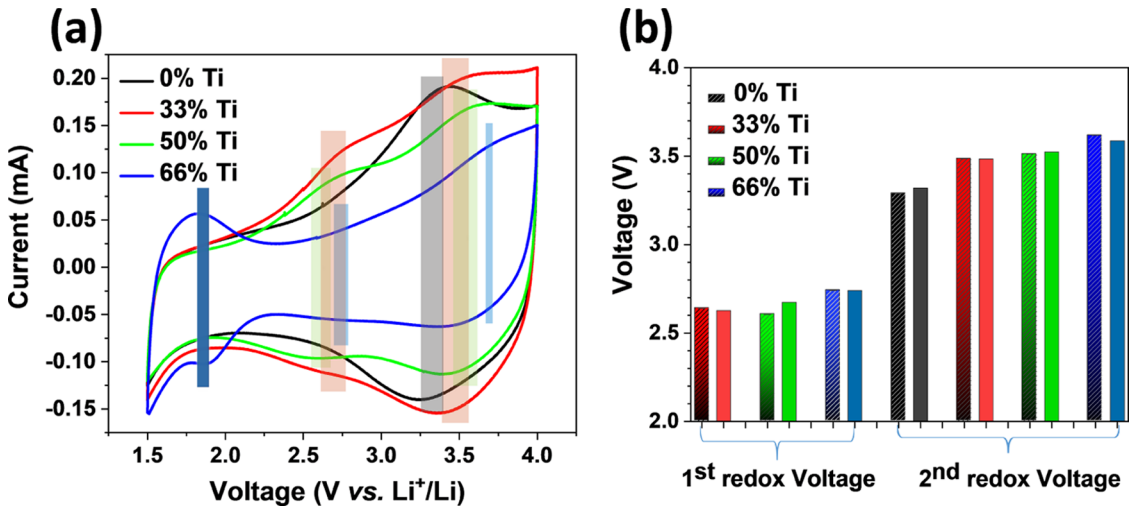

Figure 8. Cyclic voltammograms (a) and comparison of the 1st (Mn^{3+}/Mn^{2+}) and 2nd (Mn^{4+}/Mn^{3+}) redox potentials for Mn (b) extracted from dQ/dV (dashed column) and cyclic voltammetry (solid column) plots for the four samples (0% Ti, 33% Ti, 50% Ti, and 66% Ti) at a scan rate of 0.5 mV s^{-1}.

frequency mass-transfer process (W_s), which is usually shown as a Warburg-type inclined tail.[48] All capacitive components are modeled using the constant-phase element (CPE) due to the rough and porous surface of the electrode. For 66% Ti, due to the large resistance and strong overlapping between medium- and high-frequency contribution, it is not possible to distinguish the charge-transfer and mass-transfer processes; therefore, the fitted R_{ct} values were not taken into account (more data of the fitting is provided in the SI).

EIS measurements reveal then that all of the four samples present an increase in impedance upon electrochemical cycling. Several additional responses are obviously overlapped due at least to one surface layer. The total resistances after the first cycle were 49, 38, 195, and 270 Ω for the four compounds (0% Ti, 33% Ti, 50% Ti, and 66% Ti samples, respectively), which increase to 341, 176, 510, and 2390 Ω after 40 cycles, respectively. The increase in charge-transfer resistance is possibly connected to structural changes on the surface.[50] Furthermore, after 40 cycles, a shift in the intercept of the depressed semicircle with the Z_{re}-axis is observed toward a higher value, representing an increase in the ohmic resistance (from 6.5 to 13.6 Ω), which is assigned to a change of the electrolyte resistance.

Additionally, the 50% Ti sample in comparison with the 33% Ti sample shows more increase in impedance by cycling, which supports the hypothesis with regard to the instability of the 50% Ti electrode mentioned earlier. Less increase in impedance after cycling is a sign of better electrode kinetics.[51] The distinguished capacity retention for this electrode (33% Ti) could then suggest the formation of a more stable electrode−electrolyte interface during cycling.

The (de)lithiation kinetic processes were studied further by carrying out rate capability tests within 1.5−4.3 V for the four electrodes (Figure 7). While the voltage window remained the same, the electrodes were cycled at varying current rates from 0.1C to 1C. As expected, the capacity of all four electrodes decreased with increasing current rate, and the Coulombic efficiency increased due to the shorter interaction of the active material with the electrolyte at higher potentials.[40] The decrease in charge/discharge capacity as a result of the increase in the C-rate is due to the inhibition of insertion/extraction of Li^+ cations originating from diffusion barriers and the increase in surface polarization.[52] However, from the trends, it can be seen that the capacity loss mostly occurs during charge. Overall, the four electrodes demonstrate promising rate capability since by decreasing the rate from 1C back to 0.1C, the cathode materials show notable capacity retention (>90%). The 50% Ti sample shows the highest discharge capacity at all rates, while the sample with 33% Ti shows the best stability in charge and discharge at different C-rates (Figure 7). Low charge−discharge polarization with better electronic conductivity can also be noticed for the 66% Ti sample.

To identify of the working potentials and possible redox activities, differential capacity plots were extracted (dQ/dV vs voltage) for all samples (Figure S4) and compared with CV measurements (Figure 8). The derived curves reveal that two potential areas with high charge flux can be distinguished for the Ti-containing samples (at around 3.5 and 2.6 V), which point to two successive redox reactions (Mn^{2+}−Mn^{3+} and Mn^{3+}−Mn^{4+}). In contrast, the 0% Ti sample shows only one maximum (around 3.3 V), which corresponds to one redox reaction during charge transfer. However, it should be noted that due to the Jahn−Teller effect, the Mn^{4+}/Mn^{3+} redox couple can only be partially used, which could limit the expected capacity.[53] Furthermore, for the 66% Ti sample, an additional redox process below 2 V can be distinguished, owing to the presence of an amount of Ti^{3+}. This is in agreement with the prediction that Ti^{4+}−Mn^{2+} charge compensation is favored during synthesis starting from Ti^{3+}−Mn^{3+} states. The differences between the redox voltages of the four compounds are probably due to different redox couples that take part in the Li ion insertion reaction.[54] The voltage deviation between charge and discharge in the dQ/dV plots may have kinetic origins resulting from several factors such as surface energy, nanocrystallinity, and ionic diffusion.[55] Furthermore, an increasing degree of disorder during the charge and discharge process can influence Li diffusion upon cycling, which can increase the kinetic polarization as can be seen for the sample with 50% Ti.[16,56]

To further assess these statements, CV scans were recorded. The Mn^{2+}−Mn^{4+} double redox reaction of the compounds

https://doi.org/10.1021/acs.chemmater.1c02334
Chem. Mater. 2021, 33, 8235−8247

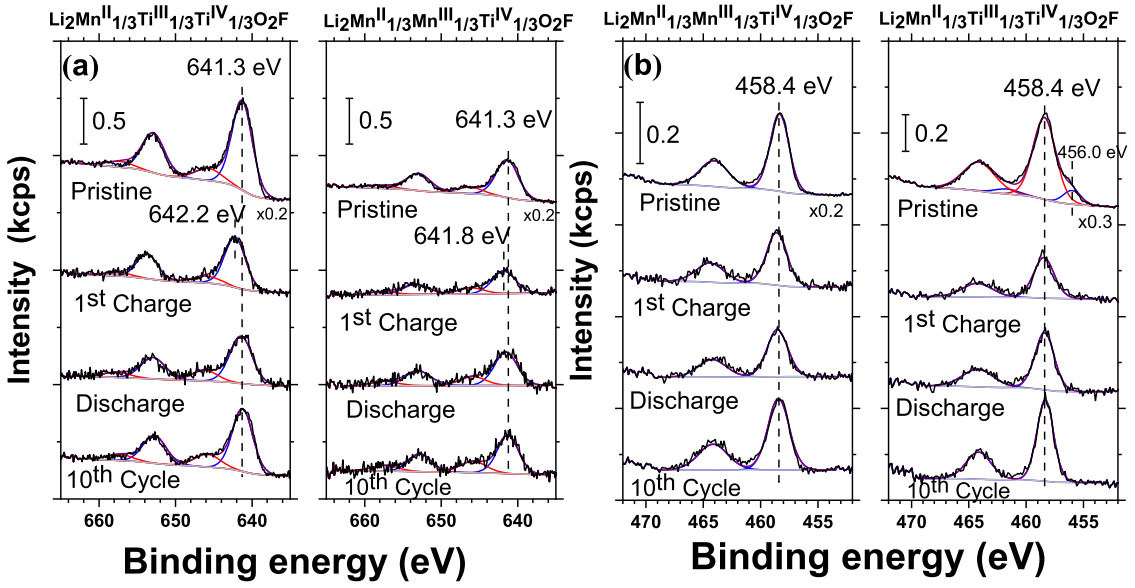

Figure 9. Mn 2p (a) and Ti 2p (b) detail spectra of the electrode samples with 33% Ti (left column) and 66% Ti (right column) at different stages of electrochemical cycling (as indicated in the figure).

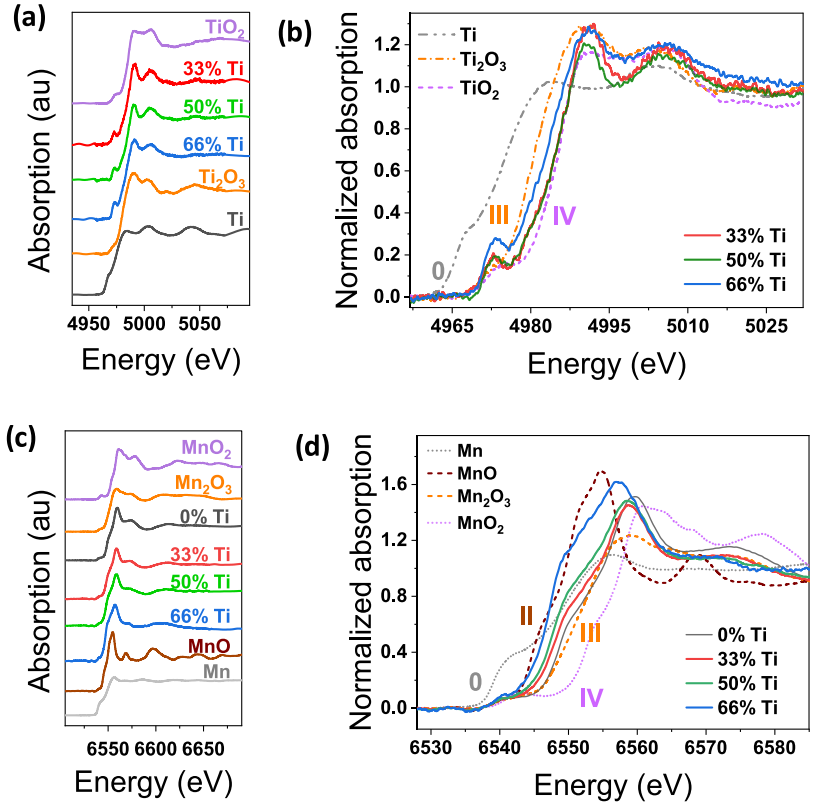

Figure 10. (a) Ti *K*-edge XANES spectra of pristine 33, 50, and 66% Ti samples with reference standards. (b) The energy shifts of the Ti *K*-edge upon composition evolution, i.e., Ti content. Ti_2O_3 and TiO_2 are used as standards for the Ti^{3+} and Ti^{4+} oxidation states. (c) Mn *K*-edge XANES spectra of 0, 33, 50, and 66% Ti pristine compounds with reference standards. (d) The Mn *K*-edge shifts with the Mn content (100 − % Ti). MnO, Mn_2O_3, and MnO_2 are used as standards for Mn^{2+}, Mn^{3+}, and Mn^{4+}, respectively.

with Ti (33% Ti, 50% Ti, and 66% Ti) can be well identified based on the working potentials (Figure 8a). Upon increasing the Ti amount, both redox peaks are slightly shifted to higher voltages (Figure 8b). These changes can be assigned most probably to modification in the chemical environment/potential, depending on the composition of each sample.[54] The half-wave potential deviation and working potential hysteresis, which is visible between the oxidized and reduced states, can be attributed to the kinetic barrier and diffusion process limitations, as discussed above for the d*Q*/d*V* curves. Furthermore, the irreversibility of the redox reactions can cause deviation between redox voltages (Figure 8b).

Oxidation State Characterization. XPS measurements were carried out to elucidate the changes in the chemical states

https://doi.org/10.1021/acs.chemmater.1c02334
Chem. Mater. 2021, 33, 8235−8247

(oxidation states) of Ti and Mn during electrochemical cycling. More precisely, the 33% (Ti-poor) and 66% (Ti-rich) samples were selected and analyzed at four different stages of cycling: in the pristine state (initial), after the 1st charge, after the 1st discharge, and after the completion of the 10th cycle (discharged state). Figure 9a shows the Mn 2p core-level spectra of these samples. The spectra of the pristine electrodes show for both compositions a main Mn 2p peak doublet with the Mn $2p_{3/2}$ peak at 641.3 eV together with a satellite peak at ∼646 eV. The position of the main peak is in the range that is usually expected for Mn(II) or Mn(III) species (between 641 and 641.5 eV). To decide between these two possibilities, we also measured the Mn 3s peak since it was demonstrated previously that the degree of the multiplet splitting of this peak can be diagnostic for the Mn oxidation state. For oxides with different Mn oxidation states (from MnO to MnO_2), a splitting of ∼6 eV was found for Mn(II), decreasing to ∼5.5 eV for Mn(III) and ∼4.8 eV for Mn^{4+}.[57,58] In our case, the spectra of both pristine samples showed a peak splitting of 6.0 eV. Therefore, the predominant oxidation state of Mn in the pristine samples is most probably + II. It should be noted that a mixture of Mn(II)/Mn(III) would have been expected for the sample with 33% Ti based on the stoichiometry ($Li_2Ti_{1/3}Mn_{2/3}O_2F$). Indeed, supplementary EXAFS measurements (Figure 10) showed the Mn *K*-edge of this sample between Mn(II) and Mn(III), indicating the coexistence of these two Mn oxidation states for this sample. The different results from XPS and EXAFS measurements can be attributed most likely to a change of the Mn oxidation state with increasing sample depth from predominantly Mn(II) at the surface (as detected by the surface-sensitive method XPS) to a mixture of Mn(II)/Mn(III) in deeper layers (measured by EXAFS). After the 1st charge, a shift of the main Mn $2p_{3/2}$ peak to 642.2 eV (33% Ti) and to 641.8 eV (66% Ti) was observed, which indicates a change in the chemical surrounding of Mn upon charging. Usually, the peak shift to higher binding energy (BE) can be linked to an increasing Mn oxidation state, which is in agreement with electrochemical data, although it is difficult to assess this change quantitatively by surface analysis. The measurements in the Mn 3s region revealed only a minor reduction of the peak splitting to 5.9 and 5.8 eV for the samples with 33 and 66% Ti, respectively (Figure S5). It should be noted that it cannot be excluded that a larger reduction of the splitting is counteracted by effects that work in another direction (see below). Nonetheless, analysis corroborates the observed shift to a higher voltage in CV for the 66% Ti sample, which may suppose that Mn^{4+} had not completely formed.

The measurements after the 1st discharge indicate essentially the return of Mn back to a lower oxidation state in both samples, with a downshift of the Mn $2p_{3/2}$ peaks and an increase of the Mn 3s peak splitting. Interestingly, the latter not only returned to 6.0 eV but also widened to 6.2 and 7.2 eV for the samples with 33 and 66% Ti, respectively. It can be speculated that this increased peak splitting is caused by an irreversible modification, such as 1st cycle interface activation, of the chemical surrounding of the Mn atoms in the electrode materials upon electrochemical cycling since it was reported before that a change in the ligands of Mn complexes (with the same Mn oxidation state) also affects the peak splitting to some extent.[59] Finally, the Mn 2p spectra recorded after 10 cycles (discharged state) show a further minor shift to lower BE for both samples (Mn $2p_{3/2}$ at 641.2 eV), which is, however, within the error margin of the measurements, while the splitting of the Mn 3s peak increases further to 6.5 and ∼8 eV for the samples with 33 and 66% Ti, respectively. These results point at further changes, mainly for the 66% Ti sample, in the chemical surrounding of the Mn atoms in the materials upon prolonged cycling. Based on the fact that Mn(I) is less plausible, it may be speculated that O-deficient regions may have formed at the surface of the particles.

The results of the measurements in the Ti 2p region are presented in Figure 9b. The spectra of the pristine electrode with 33% Ti show only one Ti 2p peak doublet (Ti $2p_{3/2}$ peak at 458.4 eV), which can be attributed to fully oxidized Ti^{4+}.[60] In contrast, an additional peak doublet at lower BE (Ti $2p_{3/2}$ peak at 456.0 eV) can be detected in the spectrum of the sample with 66% Ti, which is due to a certain amount of Ti^{3+} in this sample, as already mentioned above.[60] Finally, for all cycled samples, the peak doublet of fully oxidized Ti^{4+} is the main feature, indicating that Ti stays fully oxidized in the following and at all stages of cycling. However, due to the instability of the 66% Ti sample during cycling, it is difficult to ascertain the reversibility of Ti^{3+}, which was present initially in the sample.

Surface chemical analysis has been supplemented by X-ray absorption spectroscopy characterization of bulk samples. Figure 10a shows the Ti *K*-edge X-ray absorption near-edge structure (XANES) for pristine $Li_2Mn_{1-x}Ti_xO_2F$ with 33, 50, and 66% Ti. By "fingerprint" comparison with the standards, the 33 and 50% Ti samples show an energy position of the rising edge close to that of TiO_2 (Ti^{4+} reference), while the 66% Ti sample exhibits an edge shift toward Ti_2O_3 (Ti^{3+} reference) at lower energy, as shown in Figure 10b with better clarity. This result suggests a formal oxidation state close to IV for the 33 and 50% Ti compounds, in which the predominant amount of Ti ions is in the Ti^{4+} states. On the other hand, with increasing Ti content, the 66% Ti compound shows a mixed Ti^{3+}/Ti^{4+} valence state, which is in agreement with the XPS observation and CV analysis. Although the exact content of each valence state cannot be quantified due to the limited data quality, the relative energy position of the *K*-edge in the 66% Ti sample implies that the amount of Ti^{3+} is not negligible. It is worth noting that the commonly observed four pre-edge peaks in anatase TiO_2[61] are not distinguishable in our study, probably due to instrument limitations on the lower energy side. Therefore, it is not yet clear whether the observed single pre-edge peak could represent the distorted TiO_6 octahedral coordination[61,62] with F substitution. Future studies using more powerful synchrotron X-ray radiation shall help to clarify this structural feature.

Figure 10c,d shows the Mn *K*-edge XANES spectra of pristine $Li_2Mn_{1-x}Ti_xO_2F$ with 0, 33, 50, and 66% Ti. The edge energy position of 0% Ti is close to that of Mn_2O_3, and the 66% Ti sample displays an edge close to MnO, indicating a formal oxidation state of +3 in 0% Ti and +2 in 66% Ti, and the latter is in agreement with the XPS observation. On the other hand, both 33 and 50% Ti pristine compounds demonstrate mixed (+2−+3) oxidation states. The 50% Ti sample shows an edge energy shift closer to MnO, suggesting a larger amount of Mn(II) in this composition compared to the 33% Ti sample.

Taken together, these results support our hypothesis that Ti atoms in the pristine samples are in their preferred oxidation state IV. Only for Ti-rich samples (e.g., with 66% Ti), some Ti atoms can be found in oxidation state III. The preference for

https://doi.org/10.1021/acs.chemmater.1c02334
Chem. Mater. 2021, 33, 8235−8247

oxidation state IV is also found during cycling. Conversely, the preference of Ti for oxidation state IV leads the Mn atoms in mixed oxyfluorides to assume oxidation state II, which contributes to the high capacity of oxyfluoride materials. In addition, the present study confirms the limited contribution of Ti to the redox capacity in DRS oxyfluorides, while it anyway allows reaching better stability and achieving high electrochemical storage capacity via the Mn^{4+}/Mn^{2+} double redox activity.

CONCLUSIONS

Four different $Li_2Mn_{1-x}Ti_xO_2F$ ($0 \le x \le 2/3$) compositions were synthesized using high-energy mechanochemical ball milling and investigated as potential cathodes for Li-ion battery applications. We have first shown that Ti substitution can improve both the structural stability, providing a rigid framework structure, and the electrochemical properties of DRS oxyfluorides. Since Ti is redox inactive in the optimized structure, it appears essential for high capacity, where Mn in the pristine material is in oxidation state II, enabling a two-step redox reaction from Mn^{2+} to Mn^{4+}. By adding a certain amount of Ti in the structure, the charge gained from the first redox reaction, which is assumed to be related to the Mn^{3+}/Mn^{2+} couple, also increased. The capacity fading during cycling may assume to be the result of irreversible manganese dissolution and/or electrolyte decomposition during cycling, depending on the electrode composition. For instance, Ti-rich compositions manifested O-oxidation and cycling instability, probably due to the presence of Ti with a lower oxidation state, where Mn^{3+} is oxidized only partially. However, we found that the new composition $Li_2Mn_{2/3}Ti_{1/3}O_2F$ results in considerably improved electrochemical performance (cyclability and rate capability) and stability (lowest cell internal resistance and polarization). It can be deduced that the Ti/(Mn + Ti) atomic ratio of 33%, with high atomic miscibility in the Ti−Mn phase diagram, may play a key role in the structural stability of the composition $Li_2Mn_{2/3}Ti_{1/3}O_2F$. With the optimized Ti content, capacity retentions of 192 mAh g^{-1} (~653 Wh kg^{-1}) after 100 cycles and 136 mAh g^{-1} (~462 Wh kg^{-1}) after 200 cycles were obtained, which may open up on further material improvements and cell engineering for such a class of cathode materials, featuring a good compromise between energy and power densities.

ASSOCIATED CONTENT

Supporting Information

The Supporting Information is available free of charge at https://pubs.acs.org/doi/10.1021/acs.chemmater.1c02334.

Comparison of X-ray diffraction patterns upon Ti addition; SEM images and the corresponding EDX mapping and particle size distribution for different samples; Nyquist plot of the EIS measured after the 2nd and 40th cycles; differential capacity (dQ/dV) plots; XPS spectra in the Mn 3s region; detailed structural parameters; and quantification analysis (EDX, ICP-OES) for pristine materials and after prolonged cycling (PDF)

AUTHOR INFORMATION

Corresponding Authors

Abdel El Kharbachi − *Helmholtz Institute Ulm (HIU) Electrochemical Energy Storage, 89081 Ulm, Germany;* orcid.org/0000-0003-4332-1544; Email: kharbachi@kit.edu

Maximilian Fichtner − *Helmholtz Institute Ulm (HIU) Electrochemical Energy Storage, 89081 Ulm, Germany; Institute of Nanotechnology, Karlsruhe Institute of Technology (KIT), 76021 Karlsruhe, Germany;* Email: m.fichtner@kit.edu

Authors

Yasaman Shirazi Moghadam − *Helmholtz Institute Ulm (HIU) Electrochemical Energy Storage, 89081 Ulm, Germany*

Thomas Diemant − *Helmholtz Institute Ulm (HIU) Electrochemical Energy Storage, 89081 Ulm, Germany*

Georgian Melinte − *Helmholtz Institute Ulm (HIU) Electrochemical Energy Storage, 89081 Ulm, Germany; Institute of Nanotechnology, Karlsruhe Institute of Technology (KIT), 76021 Karlsruhe, Germany*

Yang Hu − *Helmholtz Institute Ulm (HIU) Electrochemical Energy Storage, 89081 Ulm, Germany*

Complete contact information is available at: https://pubs.acs.org/10.1021/acs.chemmater.1c02334

Author Contributions

The manuscript was written through contributions of all authors. All authors have given approval to the final version of the manuscript.

Notes

The authors declare no competing financial interest.

ACKNOWLEDGMENTS

This work contributes to the research performed at CELEST (Center for Electrochemical Energy Storage Ulm-Karlsruhe) and was partially funded by the German Research Foundation (DFG) under Project ID 390874152 (POLiS Cluster of Excellence). The TEM characterization experiments were performed at the Karlsruhe Nano Micro Facility (KNMF), a Helmholtz research infrastructure operated at KIT. Y.S.M. thanks T. Braun for assistance in SEM analysis.

REFERENCES

(1) Lu, Z.; MacNeil, D.; Dahn, J. Layered $Li[Ni_xCo_{1-2x}Mn_x]O_2$ Cathode materials for lithium-ion batteries. *Electrochem. Solid-State Lett.* **2001**, *4*, A200.

(2) Lee, J.; Kitchaev, D. A.; Kwon, D.-H.; Lee, C.-W.; Papp, J. K.; Liu, Y.-S.; Lun, Z.; Clement, R. J.; Shi, T.; McCloskey, B. D.; et al. Reversible Mn 2+/Mn 4+ double redox in lithium-excess cathode materials. *Nature* **2018**, *556*, 185−190.

(3) Lu, Z.; Dahn, J. R. Understanding the anomalous capacity of Li/Li [Ni x Li (1/3− 2x/3) Mn (2/3− x/3)] O2 cells using in situ X-ray diffraction and electrochemical studies. *J. Electrochem. Soc.* **2002**, *149*, A815.

(4) Robertson, A. D.; Bruce, P. G. Mechanism of electrochemical activity in Li2MnO3. *Chem. Mater.* **2003**, *15*, 1984−1992.

(5) Johnson, C.; Kim, J.; Lefief, C.; Li, N.; Vaughey, J.; Thackeray, M. The significance of the Li2MnO3 component in 'composite' xLi2MnO3·(1− x)LiMn0.5Ni0.5O2 electrodes. *Electrochem. Commun.* **2004**, *6*, 1085−1091.

(6) Bréger, J.; Jiang, M.; Dupré, N.; Meng, Y. S.; Shao-Horn, Y.; Ceder, G.; Grey, C. P. High-resolution X-ray diffraction, DIFFaX, NMR and first principles study of disorder in the Li2MnO3−Li [Ni1/2Mn1/2] O2 solid solution. *J. Solid State Chem.* **2005**, *178*, 2575−2585.

(7) Yabuuchi, N.; Hara, R.; Kajiyama, M.; Kubota, K.; Ishigaki, T.; Hoshikawa, A.; Komaba, S. New O2/P2-type Li-Excess Layered

Manganese Oxides as Promising Multi-Functional Electrode Materials for Rechargeable Li/Na Batteries. *Adv. Energy Mater.* **2014**, *4*, No. 1301453.
(8) Chen, R.; Ren, S.; Knapp, M.; Wang, D.; Witter, R.; Fichtner, M.; Hahn, H. Disordered Lithium-Rich Oxyfluoride as a Stable Host for Enhanced Li+ Intercalation Storage. *Adv. Energy Mater.* **2015**, *5*, No. 1401814.
(9) Chen, R.; Ren, S.; Yavuz, M.; Guda, A. A.; Shapovalov, V.; Witter, R.; Fichtner, M.; Hahn, H. Li+ intercalation in isostructural Li2VO3 and Li2VO2F with O2− and mixed O2−/F− anions. *Phys. Chem. Chem. Phys.* **2015**, *17*, 17288−17295.
(10) Nitta, N.; Wu, F.; Lee, J. T.; Yushin, G. Li-ion battery materials: present and future. *Mater. Today* **2015**, *18*, 252−264.
(11) Yabuuchi, N. Solid-state redox reaction of oxide ions for rechargeable batteries. *Chem. Lett.* **2017**, *46*, 412−422.
(12) Assat, G.; Delacourt, C.; Dalla Corte, D. A.; Tarascon, J.-M. Practical assessment of anionic redox in Li-rich layered oxide cathodes: a mixed blessing for high energy Li-ion batteries. *J. Electrochem. Soc.* **2016**, *163*, A2965.
(13) Freire, M.; Kosova, N. V.; Jordy, C.; Chateigner, D.; Lebedev, O.; Maignan, A.; Pralong, V. A new active Li−Mn−O compound for high energy density Li-ion batteries. *Nat. Mater.* **2016**, *15*, 173−177.
(14) Euchner, H.; Chang, J. H.; Groß, A. On stability and kinetics of Li-rich transition metal oxides and oxyfluorides. *J. Mater. Chem. A* **2020**, *8*, 7956−7967.
(15) Abdellahi, A.; Urban, A.; Dacek, S.; Ceder, G. Understanding the effect of cation disorder on the voltage profile of lithium transition-metal oxides. *Chem. Mater.* **2016**, *28*, 5373−5383.
(16) Lee, J.; Urban, A.; Li, X.; Su, D.; Hautier, G.; Ceder, G. Unlocking the Potential of Cation-Disordered Oxides for Rechargeable Lithium Batteries. *Science* **2014**, *343*, 519−522.
(17) Urban, A.; Lee, J.; Ceder, G. The configurational space of rocksalt-type oxides for high-capacity lithium battery electrodes. *Adv. Energy Mater.* **2014**, *4*, No. 1400478.
(18) Kang, K.; Meng, Y. S.; Breger, J.; Grey, C. P.; Ceder, G. Electrodes with high power and high capacity for rechargeable lithium batteries. *Science* **2006**, *311*, 977−980.
(19) Van der Ven, A.; Bhattacharya, J.; Belak, A. A. Understanding Li diffusion in Li-intercalation compounds. *Acc. Chem. Res.* **2013**, *46*, 1216−1225.
(20) Van der Ven, A.; Ceder, G. Lithium diffusion in layered Li_xCoO_2. *Electrochem. Solid-State Lett.* **1999**, *3*, 301.
(21) Rong, Z.; Malik, R.; Canepa, P.; Sai Gautam, G.; Liu, M.; Jain, A.; Persson, K.; Ceder, G. Materials design rules for multivalent ion mobility in intercalation structures. *Chem. Mater.* **2015**, *27*, 6016−6021.
(22) Richards, W. D.; Dacek, S. T.; Kitchaev, D. A.; Ceder, G. Fluorination of lithium-excess transition metal oxide cathode materials. *Adv. Energy Mater.* **2018**, *8*, No. 1701533.
(23) Takeda, N.; Hoshino, S.; Xie, L.; Chen, S.; Ikeuchi, I.; Natsui, R.; Nakura, K.; Yabuuchi, N. Reversible Li storage for nanosize cation/anion-disordered rocksalt-type oxyfluorides: LiMoO2−x LiF ($0 \leq x \leq 2$) binary system. *J. Power Sources* **2017**, *367*, 122−129.
(24) Jouanneau, S.; Dahn, J. Influence of LiF Additions on $Li[Ni_xCo_{1-2x}Mn_x]O_2$ Materials: Sintering, Structure, and Lithium Insertion Properties. *J. Electrochem. Soc.* **2004**, *151*, A1749.
(25) Zhu, L.; Liu, Y.; Wu, W.; Wu, X.; Tang, W.; Wu, Y. Surface fluorinated LiNi 0.8 Co 0.15 Al 0.05 O 2 as a positive electrode material for lithium ion batteries. *J. Mater. Chem. A* **2015**, *3*, 15156−15162.
(26) Seo, D.-H.; Lee, J.; Urban, A.; Malik, R.; Kang, S.; Ceder, G. The structural and chemical origin of the oxygen redox activity in layered and cation-disordered Li-excess cathode materials. *Nat. Chem.* **2016**, *8*, 692.
(27) Ji, H. W.; Wu, J. P.; Cai, Z. J.; Liu, J.; Kwon, D. H.; Kim, H.; Urban, A.; Papp, J. K.; Foley, E.; Tian, Y. S.; et al. Ultrahigh power and energy density in partially ordered lithium-ion cathode materials. *Nat. Energy* **2020**, *5*, 213−221.
(28) Baláž, P.; Achimovicova, M.; Balaz, M.; Billik, P.; Cherkezova-Zheleva, Z.; Criado, J. M.; Delogu, F.; Dutkova, E.; Gaffet, E.; Gotor, F. J.; et al. Hallmarks of mechanochemistry: from nanoparticles to technology. *Chem. Soc. Rev.* **2013**, *42*, 7571−7637.
(29) Suryanarayana, C. Mechanical alloying and milling. *Prog. Mater. Sci.* **2001**, *46*, 1−184.
(30) Cardoso, L.; Cox, D.; Hewston, T.; Chamberland, B. Structural studies of Li0.7VO2 in the temperature range 20−300 °C. *J. Solid State Chem.* **1988**, *72*, 234−243.
(31) Urban, A.; Abdellahi, A.; Dacek, S.; Artrith, N.; Ceder, G. Electronic-structure origin of cation disorder in transition-metal oxides. *Phys. Rev. Lett.* **2017**, *119*, No. 176402.
(32) Jahrman, E. P.; Holden, W. M.; Ditter, A. S.; Mortensen, D. R.; Seidler, G. T.; Fister, T. T.; Kozimor, S. A.; Piper, L. F. J.; Rana, J.; Hyatt, N. C.; et al. An improved laboratory-based X-ray absorption fine structure and X-ray emission spectrometer for analytical applications in materials chemistry research. *Rev. Sci. Instrum.* **2019**, *90*, No. 024106.
(33) Ravel, B.; Newville, M. ATHENA, ARTEMIS, HEPHAESTUS: data analysis for X-ray absorption spectroscopy using IFEFFIT. *J. Synchrotron Radiat.* **2005**, *12*, 537−541.
(34) Newville, M. Larch: An Analysis Package for XAFS and Related Spectroscopies. *J. Phys.: Conf. Ser.* **2013**, *430*, No. 012007.
(35) Baur, C.; Kallquist, I.; Chable, J.; Chang, J. H.; Johnsen, R. E.; Ruiz-Zepeda, F.; Ateba Mba, J. M.; Naylor, A. J.; Garcia-Lastra, J. M.; Vegge, T.; et al. Improved cycling stability in high-capacity Li-rich vanadium containing disordered rock salt oxyfluoride cathodes. *J. Mater. Chem. A* **2019**, *7*, 21244−21253.
(36) Lun, Z. Y.; Ouyang, B.; Cai, Z. J.; Clement, R.; Kwon, D. H.; Huang, J. P.; Papp, J. K.; Balasubramanian, M.; Tian, Y. S.; McCloskey, B. D.; et al. Design Principles for High-Capacity Mn-Based Cation-Disordered Rocksalt Cathodes. *Chem* **2020**, *6*, 153−168.
(37) Yabuuchi, N.; Takeuchi, M.; Nakayama, M.; Shiiba, H.; Ogawa, M.; Nakayama, K.; Ohta, T.; Endo, D.; Ozaki, T.; Inamasu, T.; Sato, K.; Komaba, S. High-capacity electrode materials for rechargeable lithium batteries: Li3NbO4-based system with cation-disordered rocksalt structure. *Proc. Natl. Acad. Sci. U.S.A.* **2015**, *112*, 7650−7655.
(38) Wang, R.; Li, X.; Liu, L.; Lee, J.; Seo, D.-H.; Bo, S.-H.; Urban, A.; Ceder, G. A disordered rock-salt Li-excess cathode material with high capacity and substantial oxygen redox activity: Li1. 25Nb0. 25Mn0. 5O2. *Electrochem. Commun.* **2015**, *60*, 70−73.
(39) Yabuuchi, N.; Nakayama, M.; Takeuchi, M.; Komaba, S.; Hashimoto, Y.; Mukai, T.; Shiiba, H.; Sato, K.; Kobayashi, Y.; Nakao, A.; et al. Origin of stabilization and destabilization in solid-state redox reaction of oxide ions for lithium-ion batteries. *Nat. Commun.* **2016**, *7*, No. 13814.
(40) Baur, C.; Chable, J.; Klein, F.; Chakravadhanula, V. S. K.; Fichtner, M. Reversible delithiation of disordered rock salt LiVO2. *ChemElectroChem* **2018**, *5*, 1484−1490.
(41) Amatucci, G.; Tarascon, J.-M. Optimization of Insertion Compounds Such as LiMn2 O 4 for Li-Ion Batteries. *J. Electrochem. Soc.* **2002**, *149*, K31.
(42) Komaba, S.; Kumagai, N.; Sasaki, T.; Miki, Y. Manganese dissolution from lithium doped Li-Mn-O spinel cathode materials into electrolyte solution. *Electrochemistry* **2001**, *69*, 784−787.
(43) Shirazi moghadam, Y.; Masoudpanah, S. M.; Alamolhoda, S.; Daneshtalab, R. Electrochemical properties of LiMn1.5Ni0.5O4 powders synthesized by solution combustion method: Effect of CTAB as a fuel. *Adv. Powder Technol.* **2020**, *31*, 639−644.
(44) Maier, J. Ionic conduction in space charge regions. *Prog. Solid State Chem.* **1995**, *23*, 171−263.
(45) Kitaoka, S.; Inoue, N. The effect of dispersed SrTiO3 particles on the ionic conduction of (La, Li) Ti2O6. *Solid State Ionics* **2009**, *180*, 598−601.
(46) Mei, A.; Wang, X.-L.; Lan, J.-L.; Feng, Y.-C.; Geng, H.-X.; Lin, Y.-H.; Nan, C.-W. Role of amorphous boundary layer in enhancing ionic conductivity of lithium−lanthanum−titanate electrolyte. *Electrochim. Acta* **2010**, *55*, 2958−2963.

https://doi.org/10.1021/acs.chemmater.1c02334
Chem. Mater. 2021, 33, 8235−8247

(47) Chen, R.; Maawad, E.; Knapp, M.; Ren, S.; Beran, P.; Witter, R.; Hempelmann, R. Lithiation-driven structural transition of VO 2 F into disordered rock-salt Li x VO 2 F. *RSC Adv.* **2016**, *6*, 65112−65118.
(48) Aurbach, D.; Levi, M. D.; Levi, E.; Teller, H.; Markovsky, B.; Salitra, G.; Heider, U.; Heider, L. Common electroanalytical behavior of Li intercalation processes into graphite and transition metal oxides. *J. Electrochem. Soc.* **1998**, *145*, 3024.
(49) Cambaz, M. A.; Vinayan, B. P.; Euchner, H.; Pervez, S. A.; Geßwein, H.; Braun, T.; Gross, A.; Fichtner, M. Design and Tuning of the Electrochemical Properties of Vanadium-Based Cation-Disordered Rock-Salt Oxide Positive Electrode Material for Lithium-Ion Batteries. *ACS Appl. Mater. Interfaces* **2019**, *11*, 39848−39858.
(50) Cambaz, M. A.; Vinayan, B. P.; Gesswein, H.; Schiele, A.; Sarapulova, A.; Diemant, T.; Mazilkin, A.; Brezesinski, T.; Behm, R. J.; Ehrenberg, H.; et al. Oxygen Activity in Li-Rich Disordered Rock-Salt Oxide and the Influence of LiNbO3 Surface Modification on the Electrochemical Performance. *Chem. Mater.* **2019**, *31*, 4330−4340.
(51) Nakajima, M.; Yabuuchi, N. Lithium-excess cation-disordered rocksalt-type oxide with nanoscale phase segregation: Li1. 25Nb0. 25V0. 5O2. *Chem. Mater.* **2017**, *29*, 6927−6935.
(52) Shirazi moghadam, Y.; Masoudpanah, S. M.; Alamolhoda, S. Solution combustion synthesis of LiMn1.5Ni0.5O4 powders by a mixture of fuels. *Ceram. Int.* **2019**, *45*, 22849−22853.
(53) Reed, J.; Ceder, G.; Van Der Ven, A. Layered-to-spinel phase transition in LixMnO2. *Electrochem. Solid-State Lett.* **2001**, *4*, A78.
(54) Ahn, J.; Chen, D.; Chen, G. A Fluorination Method for Improving Cation-Disordered Rocksalt Cathode Performance. *Adv. Energy Mater.* **2020**, *10*, No. 2001671.
(55) Obrovac, M.; Dahn, J. Implications of finite-size and surface effects on nanosize intercalation materials. *Phys. Rev. B* **2000**, *61*, 6713.
(56) Urban, A.; Matts, I.; Abdellahi, A.; Ceder, G. Computational design and preparation of cation-disordered oxides for high-energy-density Li-ion batteries. *Adv. Energy Mater.* **2016**, *6*, No. 1600488.
(57) Oku, M.; Hirokawa, K.; Ikeda, S. X-ray photoelectron spectroscopy of manganese—oxygen systems. *J. Electron Spectrosc. Relat. Phenom.* **1975**, *7*, 465−473.
(58) Lee, J. H.; Sa, Y. J.; Kim, T. K.; Moon, H. R.; Joo, S. H. A transformative route to nanoporous manganese oxides of controlled oxidation states with identical textural properties. *J. Mater. Chem. A* **2014**, *2*, 10435−10443.
(59) Nelson, A.; Reynolds, J. G.; Christou, G. Spin-state effects on the outer core-level multiplet structures for high-spin Mn molecular clusters. *J. Appl. Phys.* **2003**, *93*, 2536−2539.
(60) Mayer, J.; Diebold, U.; Madey, T.; Garfunkel, E. Titanium and reduced titania overlayers on titanium dioxide (110). *J. Electron Spectrosc. Relat. Phenom.* **1995**, *73*, 1−11.
(61) Farges, F.; Brown, G. E.; Rehr, J. J. Ti K-edge XANES studies of Ti coordination and disorder in oxide compounds: Comparison between theory and experiment. *Phys. Rev. B* **1997**, *56*, 1809−1819.
(62) Lafont, U.; Carta, D.; Mountjoy, G.; Chadwick, A. V.; Kelder, E. M. In Situ Structural Changes upon Electrochemical Lithium Insertion in Nanosized Anatase TiO2. *J. Phys. Chem. C* **2010**, *114*, 1372−1378.

NOTE ADDED AFTER ASAP PUBLICATION

This paper published online on October 18, 2021, with an error in Figure 10's caption. The corrected version reposted with the issue on November 9, 2021.

https://doi.org/10.1021/acs.chemmater.1c02334
Chem. Mater. 2021, 33, 8235−8247